Pyroelectric energy conversion using PLZT ceramics and the ferroelectric–ergodic relaxor phase transition

2013 Smart Mater. Struct. 22 025038

(http://iopscience.iop.org/0964-1726/22/2/025038)

Smart Mater. Struct. **22** (2013) 025038 (16pp) doi:10.1088/0964-1726/22/2/025038

Pyroelectric energy conversion using PLZT ceramics and the ferroelectric–ergodic relaxor phase transition

Felix Y Lee, Hwan Ryul Jo, Christopher S Lynch and Laurent Pilon[1]

Mechanical and Aerospace Engineering Department, Henry Samueli School of Engineering and Applied Science, University of California, Los Angeles, Los Angeles, CA 90095, USA

E-mail: pilon@seas.ucla.edu

Received 10 September 2012, in final form 3 December 2012
Published 29 January 2013
Online at stacks.iop.org/SMS/22/025038

Abstract
This paper is concerned with direct conversion of waste heat into electricity by executing the Olsen cycle on lead lanthanum zirconate titanate (PLZT) ceramics undergoing a relaxor–ferroelectric phase transition. The Olsen cycle consists of two isothermal and two isoelectric field processes. First, the temperature-dependent dielectric properties were measured for *x*/65/35 PLZT. The polarization transition temperature of *x*/65/35 PLZT was found to decrease from 240 to 10 °C as *x* increased from 5 to 10 mol%. This suggests that the different compositions should be operated over different temperature ranges for maximum thermal to electrical energy conversion. The energy and power densities generated by the Olsen cycle using *x*/65/35 PLZT samples were measured by successively dipping the samples in isothermal dielectric oil baths. Large energy and power densities were obtained when the samples underwent the ergodic relaxor–ferroelectric phase transition. A maximum energy density of 1014 J l^{-1} per cycle was obtained with a 190 μm thick 7/65/35 PLZT sample cycled at 0.026 Hz between 30 and 200 °C and between 0.2 and 7.0 MV m^{-1}. To the best of our knowledge, this is the largest pyroelectric energy density ever demonstrated experimentally with ceramics, single crystals, or polymers. A maximum power density of 48 W l^{-1} was achieved using a 200 μm thick 6/65/35 PLZT sample for temperatures between 40 and 210 °C and electric fields between 0 and 8.5 MV m^{-1} at a frequency of 0.060 Hz. The maximum applied electric field and temperature swings of these materials were physically limited by dielectric breakdown and thermomechanical stress.

(Some figures may appear in colour only in the online journal)

1. Introduction

Waste heat is a necessary by-product of all thermodynamic cycles implemented in power, refrigeration, and heat pump processes [1]. In 2009, over 55% of the energy consumed from all sources in the United States was lost as low temperature waste heat, most of it discharged to the environment [2]. More than 80% of this waste heat was produced by electricity generation and transportation systems [2]. A technology for generating electric power from this free source of thermal energy could provide cost savings through increased process efficiencies [3, 4].

During the past decade, direct energy conversion technologies for harvesting low temperature waste heat have been investigated intensively. Technologies for thermal energy harvesting include Stirling engines [5], organic Rankine cycles [6, 7], thermoelectric devices [8], and pyroelectric energy conversion [4, 7, 9–27]. The Olsen cycle converts

[1] www.seas.ucla.edu/~pilon.

temporal temperature variations directly into electrical energy [9]. This generated energy can be harvested in practice by delivering it to an external load or a storage unit [28]. In order to achieve the maximum device performance, it is necessary to identify the pyroelectric material that generates the largest amount of energy and power for a given temperature range.

The present study is concerned with assessing the pyroelectric energy and power generation capabilities of lead lanthanum zirconate titanate (PLZT) with different lanthanum doping concentrations. PLZT thin films were synthesized and their temperature-dependent dielectric behavior was characterized. The effects of electric field, operating temperature, and cycle frequency on the energy generated were systematically investigated for a wide range of conditions.

2. Background

2.1. Pyroelectricity

Pyroelectric materials possess a spontaneous polarization defined as the average dipole moment per unit volume [29]. Ferroelectric materials are a subclass of pyroelectric materials. They have the ability to switch the direction and magnitude of their spontaneous polarization by reversing the external electric field [29, 30]. A ferroelectric material undergoes a ferroelectric to paraelectric phase transition when heated above the Curie temperature T_{Curie}. This phase transition temperature is typically defined as the temperature corresponding to a peak in the real component of the complex dielectric constant for a specified frequency and applied electric field [31]. The spontaneous polarization is temperature dependent and becomes negligibly small as the temperature increases beyond T_{Curie}. Figure 1 shows the bipolar isothermal hysteresis curves between electric displacement and electric field for a ferroelectric material at temperatures T_{hot} and T_{cold} [32–35]. The *D*–*E* loops travel in a counter-clockwise direction upon cycling of the electric field within the material while its temperature is held constant. The electric displacement D of an isotropic pyroelectric material at electric field E and temperature T can be expressed as [29, 36]

$$D(E, T) = \varepsilon_0 \varepsilon_{\text{r}}(E, T)E + P_{\text{s}}(T) \tag{1}$$

where ε_0 is the vacuum permittivity (=8.854 × 10^{12} F m^{-1}) and $\varepsilon_{\text{r}}(E, T)$ is the relative permittivity (or dielectric constant) of the material at electric field E and temperature T. The saturation polarization denoted by $P_{\text{s}}(T)$ is estimated as the electric displacement in the linear fit of D versus E extrapolated from a finite electric field to zero electric field as illustrated in figure 1 [37]. The slope of this linear fit is equal to the product $\varepsilon_0 \varepsilon_{\text{r}}(E, T)$. In this case, $\varepsilon_{\text{r}}(E, T)$ corresponds to the large field dielectric constant. The remnant polarization $P_{\text{r}}(T)$ is defined as the polarization under zero applied electric field and the coercive field $E_{\text{C}}(T)$ corresponds to the electric field required to reach zero polarization [38]. The critical electric field $E_{\text{cr}}(T)$ was estimated from the inflection point in the isothermal *D*–*E* loop [22].

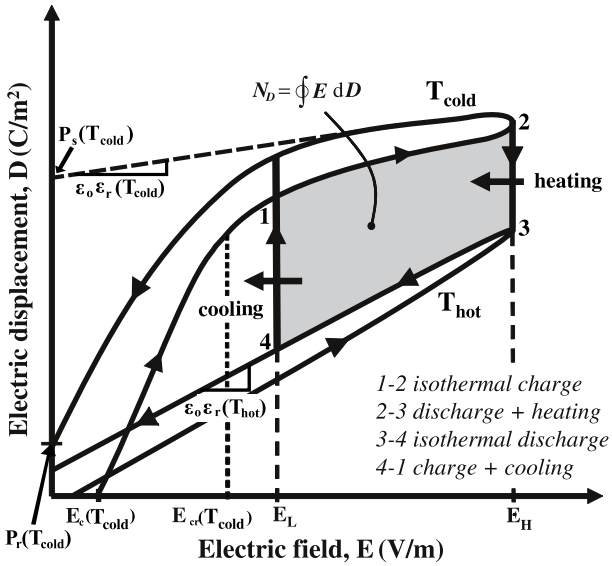

Figure 1. Isothermal bipolar electric displacement versus electric field (*D*–*E*) hysteresis loops for a typical pyroelectric material at temperatures T_{hot} and T_{cold} along with the Olsen cycle. The electrical energy generated per cycle is represented by the area enclosed between 1-2-3-4.

2.2. Olsen cycle

Figure 1 illustrates the Olsen cycle in the electric displacement versus electric field (*D*–*E*) diagram [9]. It is composed of two isothermal and two isoelectric processes. Process 1-2 consists of charging the pyroelectric element (PE) at T_{cold} by increasing the applied electric field from E_{L} to E_{H}. Process 2-3 corresponds to discharging the PE by heating it from T_{cold} to T_{hot} under constant electric field E_{H}. Process 3-4 consists of reducing the electric field from E_{H} to E_{L} under isothermal conditions at T_{hot}. Finally, Process 4-1 closes the cycle by cooling the PE from T_{hot} to T_{cold} under constant electric field E_{L}. In brief, the principle of the Olsen cycle is to charge a capacitor via cooling under low electric field and to discharge it by heating at higher electric field.

The area enclosed by the clockwise 1-2-3-4 loop in the *D*–*E* curve represents the electric energy produced per unit volume of material per cycle denoted by N_{D} (in J l^{-1} per cycle) and defined as [9]

$$N_{\text{D}} = \oint E\,dD. \tag{2}$$

The corresponding power density P_{D} (in W l^{-1}) produced by the pyroelectric element is expressed as

$$P_{\text{D}} = N_{\text{D}} f \tag{3}$$

where f is the cycle frequency. Equation (2) suggests that there are two ways to increase the generated energy and power densities including (i) increasing T_{hot} and decreasing T_{cold} and/or (ii) increasing the electric field span ($E_{\text{H}} - E_{\text{L}}$). This is limited, however, by the thermoelectromechanical stress that the sample can physically withstand.

Attempts have been made to use the pyroelectric effect to produce electricity from relatively small temperature oscillations without using the Olsen cycle [25–27, 39]. Lee

et al [34] compared these pyroelectric energy generation methods and demonstrated that performing the Olsen cycle enables one to generate significantly more power than by simply using the pyroelectric effect, regardless of the heating and cooling methods considered.

2.3. Relaxor–ferroelectric PLZT

This study investigates a relaxor–ferroelectric systems consisting of x mol% lanthanum doped into a 65 mol% lead zirconate and 35 mol% lead titanate solid solution [$Pb_{1-x}La_x(Zr_{0.65}Ti_{0.35})_{1-x/4}O_3$], abbreviated as x/65/35 PLZT. The phase diagram [40, 41] of x/65/35 PLZT ceramics at room temperature and zero electric field shows that the compositions with 5 mol% $\leq x \leq$ 9 mol% feature rhombohedral crystal symmetry and are near the rhombohedral ferroelectric–mixed ferroelectric/cubic phase boundary [41]. The phase transition of the x/65/35 PLZT system depends on the applied electric field, temperature, and frequency [31, 42–44]. It is paraelectric beyond the Burns temperature $T_B \simeq$ 350 °C corresponding to the Curie temperature of the La-free composition [45]. Upon cooling below T_B, the material transforms from paraelectric to ergodic relaxor resulting in domain alignment and enlargement of the domain correlation radius [37]. In the relaxor phase, interactions between randomly oriented polar nanodomains cause distortion in the crystal structures which gives rise to large dielectric and piezoelectric constants [46].

As domains grow and coalesce into polar clusters, random fields induced in the relaxor state become suppressed [37]. This marks a phase transition between ergodic relaxor (nanodomain) and ferroelectric (macrodomain) that is field dependent and occurs at the Curie temperature T_{Curie}. The latter can be determined from the maximum of the pyroelectric coefficient $(\partial D/\partial T)_{\sigma,E}$ versus temperature T curve measured under a specified electric field E [43, 47]. The material can revert phase from ferroelectric to ergodic relaxor by heating it above T_{Curie} and/or by de-poling it below a critical electric field $E_{cr}(T)$. In x/65/35 PLZT, the ferroelectric phase cannot be established spontaneously upon cooling under zero electric field [43]. Application of an external electric field E greater than $E_{cr}(T)$ is required to stabilize the ferroelectric phase from the ergodic relaxor phase [48–51].

The isothermal D–E loops for x/65/35 PLZT degenerate into narrow and linear loops as the temperature increases above T_{Curie} [31]. Then, the remnant polarization $P_r(T)$ and the coercive field $E_C(T)$ become negligibly small in the relaxor state compared with their values in the ferroelectric state [52]. The relaxor–ferroelectric phase transition is typically accompanied by a large change in electric displacement D. In order to produce the maximum energy and power output by a relaxor–ferroelectric material, the relaxor–ferroelectric phase transition must take place during the Olsen cycle.

2.4. Dipping experiments

Successive dipping of a PE into hot and cold dielectric fluid baths under specified electric fields provides a simple and somewhat idealized way to perform the Olsen cycle. It can be used to rapidly assess the energy and power generation performance of pyroelectric materials before using them in actual devices. Recently, Lee *et al* [53] performed the dipping experiments on relaxor–ferroelectric 8/65/35 PLZT. A maximum energy density of 888 J l^{-1} per cycle was generated at 0.0178 Hz, corresponding to a power density of 15.8 W l^{-1}, for operating temperatures between 25 and 160 °C and electric field cycled between 0.2 and 7.5 MV m^{-1}. Chin *et al* [54] performed a similar procedure on 9.5/65/35 PLZT ceramics and achieved a maximum power density of 55 W l^{-1} at 0.125 Hz. The Olsen cycle was performed between 3 and 140 °C and electric field from 0.2 to 6.0 MV m^{-1}. These studies [53, 54] demonstrated that the energy conversion performance of PLZT is strongly dependent on the material composition and operating temperatures and electric fields. In fact, T_{Curie} was reported to be −25, −10, 65, 150, 240, and 310 °C for the 65/35 Pb/Ti ratio and x = 10, 9, 8, 7, 6, and 5 mol%, respectively [55]. An increase in lanthanum dopant concentration hinders the onset of long-range ferroelectric order upon cooling [37]. This contributes to Curie temperature reduction from 310 to −25 °C as lanthanum doping level increases from 5 to 10 mol% [37]. Additionally, the remnant polarization and dielectric constant of rhombohedral ferroelectric x/65/35 PLZT were large compared to other PLZT compositions [41].

These results suggest that PLZT is a very promising pyroelectric material to employ in pyroelectric converters. The lanthanum concentration in PLZT can be advantageously adjusted in order to match the temperature range available in a particular application. The power output of pyroelectric converters implementing the Olsen cycle using conduction [27, 34, 56, 57], convection [9–13, 24, 32], or radiation [23] could also be significantly improved by employing a multistaging technique [13]. The latter consists of strategically placing a series of pyroelectric materials in the order of increasing T_{Curie} between a cold and a hot temperature source. This could be achieved by superimposing PLZT films with increasing amount of La doping. Consequently, the present study aims to experimentally evaluate the pyroelectric energy and power generation capabilities of different compositions in the relaxor–ferroelectric x/65/35 PLZT family.

3. Experiments

3.1. Material synthesis

Twelve x/65/35 PLZT ceramic samples with circular cross-sections were fabricated by the mixed oxide method [58]. They consisted of two samples for each lanthanum doping level x = 5, 6, 7, 8, 9, and 10 mol%. Figure 2 shows a block diagram summarizing the material synthesis procedure. The starting precursors included high purity (≥99.9 mol%) lead carbonate $PbCO_3$ (Hammond Lead Products Inc., Hammond, IN, USA), zirconium dioxide ZrO_2 (Magnesium Elektron Inc., Flemington, NJ, USA), lanthanum oxide La_2O_3 (Inframat Advanced Materials LLC, Manchester, CT, USA),

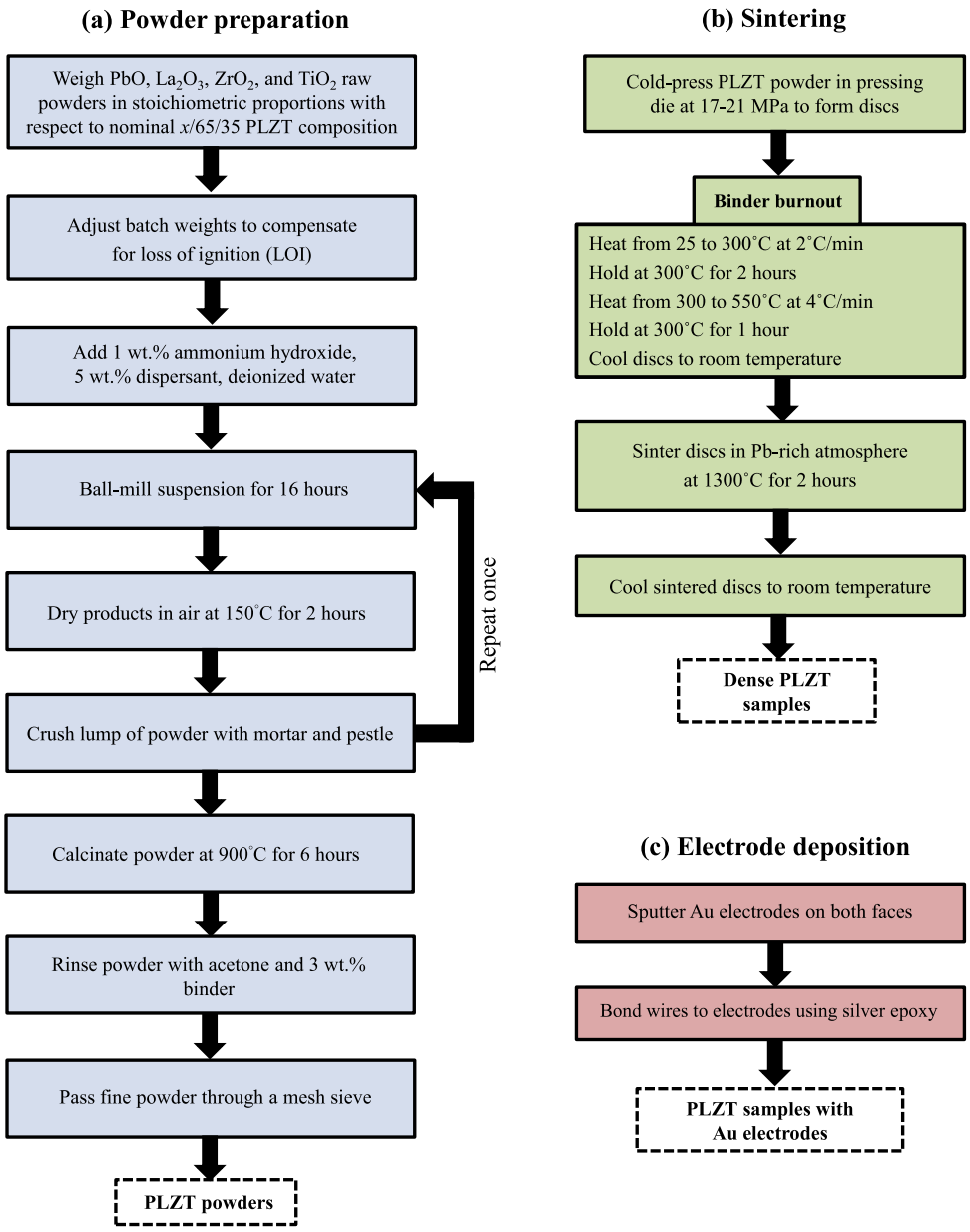

Figure 2. Procedure used to synthesize *x*/65/35 PLZT samples using the mixed oxide method. The processes include (a) powder preparation, (b) sintering, and (c) electrode deposition. The starting precursors were high purity raw powders and the final products were dense *x*/65/35 PLZT samples with Au electrodes.

and titanium dioxide TiO_2 (Ishihara Sangyo Kaisha Ltd, Japan). Each constituent was weighed in stoichiometric proportions with respect to the nominal composition of $Pb_{1-x}La_x(Zr_{0.65}Ti_{0.35})_{1-x/4}O_3$ (*x*/65/35 PLZT). The batch weights were adjusted to compensate for the weight loss on ignition (LOI) measured by heating each precursor material individually to 300 °C at 10 °C min^{-1} in an alumina crucible and then cooling it down to room temperature. Deionized water, 1 wt% ammonium hydroxide NH_4OH solution, and 5 wt% Darvan dispersant (R T Vanderbilt Company Inc., Norwalk, CT, USA) were also mixed with the powder oxides. The suspension was ball milled using zirconia grinding media for 16 h in order to increase powder homogeneity. Immediately thereafter, the slurry was poured through a strainer into a Pyrex dish and rinsed with deionized water. Then, the products were dried in an oven at 150 °C in air for 2 h. The resulting lumps of powder were crushed using an agate mortar and pestle. The milling, drying, and crushing processes were repeated once before the powders were deposited into an alumina crucible and calcined at 900 °C for 6 h.

Following this process, a 3 wt% Paraloid B-67 binder (Rohm and Haas Company, Philadelphia, PA, USA) was added to the powder using acetone as the solvent. Then, the binderized powder was passed through a 100-mesh sieve to filter aggregated powders which contribute to a low packing efficiency. Fine powders were uniaxially cold pressed into a 1.27 cm diameter pressing die (Across International LLC, Berkeley Heights, NJ, USA) at 17–21 MPa. In order to burn

Table 1. Sample thickness b, electrode cross-sectional area A, polarization transition temperature T_p, and Curie temperature T_{Curie} of the different x/65/35 PLZT samples investigated in this study.

Sample	Material	Thickness b (μm)	Electrode area A (mm^2)	T_p (°C)	T_{Curie} (°C)
1	5/65/35 PLZT	200	36.4	240	240
2	5/65/35 PLZT	180	33.2		
3	6/65/35 PLZT	180	24.6	210	180
4	6/65/35 PLZT	200	32.7		
5	7/65/35 PLZT	190	32.1	190	120
6	7/65/35 PLZT	210	32.8		
7	8/65/35 PLZT	290	17.8	140	65
8	8/65/35 PLZT	180	36.7		
9	9/65/35 PLZT	200	34.6	70	15
10	9/65/35 PLZT	210	33.4		
11	10/65/35 PLZT	180	32.8	10	—
12	10/65/35 PLZT	190	33.2		

out the binder, the specimen were heated in a chamber furnace (Carbolite Ltd, Hope Valley, UK) in two stages. First, the specimen were ramp heated from 25 to 300 °C at a rate of ~2.3 °C min^{-1} and then held at 300 °C for 2 h. Then, the samples were heated from 300 to 550 °C at ~4.1 °C min^{-1} and held at 550 °C for 1 h. Then, the discs were slowly cooled to room temperature. Once this process was completed, the specimens were sintered at 1300 °C by heating it from 25 to 1300 °C at ~10 °C min^{-1}. Then, the temperature was held at 1300 °C for 2 h in a Pb rich atmosphere provided by excess $PbCO_3$ and ZrO_2 powders (~2.5 g) to compensate for the volatile evaporative loss of lead oxide above 800 °C [59]. The excess lead ensures that the PLZT samples achieve full density by permitting a liquid phase to form in its grain boundaries during densification [59]. During the sintering process, pellets were fired onto a platinum foil to prevent diffusion of PLZT into its alumina substrate. The $PbCO_3$ and ZrO_2 powders were placed in an alumina combustion boat next to the pellets, all enclosed in an inverted alumina crucible. Finally, the specimen were cooled to room temperature to form dense PLZT ceramics.

Each x/65/35 PLZT sample was mechanically cut or sanded to achieve thicknesses ranging from 180 to 200 μm. Circular gold (Au) electrodes were sputtered onto opposite faces of the polished samples about 2 mm from the edges by using a mask. The electrode area was chosen to be smaller than the overall sample area in order to reduce electrical conduction around the sample edges [53]. Electrical wires were bonded to the electrodes using silver epoxy. Silicone conformal coating was also applied to both faces of the samples and cured at 65 °C for one hour to increase the samples' dielectric strength [60]. Table 1 summarizes the thickness and electrode cross-sectional area of each x/65/35 PLZT sample investigated in this study.

3.2. Electrical and thermal subsystems

The electrical subsystem used to measure isothermal D–E loops and to perform the Olsen cycle consisted of a modified Sawyer-Tower bridge circuit. The loads consisted of a resistor in parallel and capacitor in series with the pyroelectric sample [35]. It was used to apply the required electric field across the pyroelectric element and to measure the charge Q at the electrode surfaces. Details of the circuit used in the present study were provided in previous studies [18, 35, 53] and need not be repeated.

The thermal subsystem consisted of two beakers containing diphenyl-dimethylsiloxane dielectric fluid (Clearco DPDM-400) maintained at T_{cold} and T_{hot} [18, 35, 53]. This dielectric fluid is stable at temperatures up to 260 °C and possesses a large electrical resistivity ($\geq 10^{14}$ Ω cm) for preventing high voltage arcing to the sample [61]. Each beaker contained a magnetic stirrer to ensure uniform dielectric oil bath temperatures. The latters were monitored using K-type thermocouples and maintained at their desired value by using temperature-controlled hot plates. The samples were alternatively immersed in hot and cold baths to create time-dependent temperature oscillations required in the Olsen cycle.

The thermal time constant of PLZT samples can be estimated as $\tau = \rho c_p / hb$ [62] where h is the convective heat transfer coefficient, b is the sample thickness, while ρ and c_p are the sample density and specific heat, respectively. For example, the thermal time constant for a 200 μm thick PLZT sample was estimated to be 1.73 s assuming $\rho =$ 7900 kg m^{-3} [63], $c_p = 329$ J kg^{-1} K^{-1} [64], and $h =$ 300 W m^{-2} K^{-1} corresponding to convective quenching in an oil bath [65]. This time constant indicates that the sample reached thermal equilibrium rapidly after it was transferred from one oil bath to the other during processes 2-3 and 4-1 of the Olsen cycle.

3.3. Experimental procedure

Two independent sets of measurements were performed on each x/65/35 PLZT composition studied to identify the conditions and values of (a) the maximum energy density (Samples 1, 3, 5, 7, 9) and (b) the maximum power density (Samples 2, 4, 6, 8, 10). Figure 3 illustrates the systematic procedure used to perform these measurements. First, isothermal dielectric hysteresis loops were measured and analyzed. Then, the effects of low and high electric fields E_L and E_H on the energy and power densities were successively assessed for each sample.

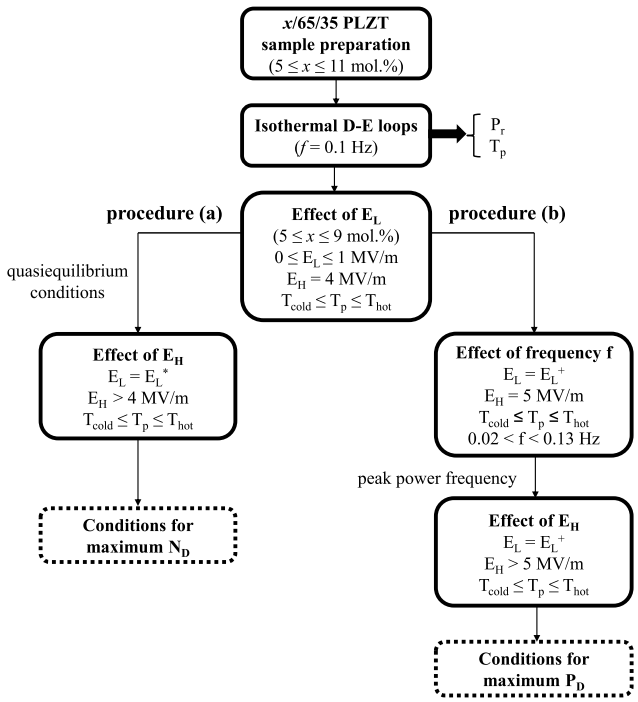

Figure 3. Systematic procedure used to identify the maximum (a) energy density N_D (Samples 1, 3, 5, 7, 9) and (b) power density P_D (Samples 2, 4, 6, 8, 10) of each PLZT composition investigated.

3.3.1. Isothermal D–E loops. Isothermal bipolar *D–E* loops were systematically collected for each sample by using the electrical circuit described in [33–35]. The *D–E* loops were measured to analyze the material's temperature-dependent dielectric behavior and to select the operating temperatures of the Olsen cycle to ensure that the ergodic relaxor–ferroelectric phase transition was captured. For *x*/65/35 PLZT with *x* ranging from 5 to 9 mol%, the measurements were taken upon heating in 10–40 °C intervals while the samples were immersed in a dielectric fluid bath maintained at constant temperature ranging from 3 to 250 °C. For 10/65/35 PLZT, the measurements were performed in (i) an insulated dewar with samples exposed to liquid oxygen maintained at temperatures between −110 and 0 °C and (ii) an isothermal oil bath kept at temperatures between 0 and 40 °C. All bipolar *D–E* loop measurements were carried out by imposing a continuous triangular voltage signal across the sample at 0.1 Hz. This frequency corresponded to that of the isothermal electric field changes during processes 1-2 and 3-4 of the Olsen cycle. The amplitude of the applied voltage corresponded to an electric field cycled between −3.0 and +3.0 MV m^{-1}.

3.3.2. Olsen cycle. The Olsen cycle was performed on all *x*/65/35 PLZT samples under various electric fields, temperatures, and frequencies to investigate their respective effects on the energy and power densities. The energy density N_D generated by the Olsen cycle and given by equation (2) was numerically estimated using the trapezoidal rule. Similarly, the power density was computed according to equation (3). The overall cycle frequency was defined as $f = (\tau_{12} + \tau_{23} + \tau_{34} + \tau_{41})^{-1}$ where τ_{ij} corresponds to the duration of process $i - j$ in the Olsen cycle. For most materials and applications, the maximum energy density and maximum power density are typically not achieved at the same operating frequency. The maximum energy density can be obtained by operating the Olsen cycle under quasiequilibrium conditions at relatively low frequencies [66]. In practice, quasiequilibrium conditions were achieved when the electric displacement reached steady state, i.e., $(\partial D/\partial t) = 0$, during processes 2-3 and 4-1 before the electric field was varied in processes 3-4 and 1-2, respectively. On the other hand, the maximum power density was typically reached at higher frequency. Therefore, the cycle frequency was varied to examine its effect on power density by changing the duration of the isoelectric field heating process 2-3 and of the cooling process 4-1 denoted by τ_{23} and τ_{41}, respectively. For example, the times τ_{23} and τ_{41} varied between approximately 2 and 15 s. However, the durations of the isothermal processes 1-2 (τ_{12}) and 3-4 (τ_{34}) were kept constant at around 1.5 s. Note that the time required to manually transfer the sample between cold and hot baths was about 0.5 s. Overall, the cycle frequency f varied between 0.024 and 0.13 Hz.

The effect of E_L on the energy and power densities produced in the Olsen cycle was assessed with the cold and hot source temperatures T_{cold} and T_{hot} determined based on *D–E* loop measurements. The high electric field was maintained at $E_H = 4.0$ MV m^{-1} while the low electric field E_L was varied between 0 and 1.0 MV m^{-1}. The low electric field corresponding to a peak in energy density denoted by E_L^*, and to a maximum power density, denoted by E_L^+, were used thereafter in each respective set of measurement.

Procedure (a) in figure 3 was followed in order to obtain the maximum energy density. The Olsen cycle was performed under quasiequilibrium conditions with low electric field E_L^* fixed and temperatures maintained at T_{cold} and T_{hot}. The high electric field E_H was increased from 4.0 MV m^{-1} in 0.5 MV m^{-1} increments until the sample suffered electromechanical breakdown. On the other hand, procedure (b) in figure 3 was followed to find the conditions for maximum power density. The power density typically reaches a maximum at a frequency larger than the frequency corresponding to the maximum energy density. Chin *et al* [54] suggested that the peak power frequency for 9.5/65/35 PLZT was dependent on the applied high electric field. Therefore, the Olsen cycle was performed at cycle frequency varying between 0.024 and 0.13 Hz with high electric field E_H set as either 5.0, 6.0, or 7.0 MV m^{-1}. The low electric field was fixed at the previously determined value of E_L^+ and temperatures T_{cold} and T_{hot} were held constant. Then, the peak power frequency was identified. Finally, the Olsen cycle was carried out at the peak power frequency for high electric field E_H raised from 5.0 MV m^{-1} in 0.5 MV m^{-1} increments until the sample experienced dielectric breakdown.

4. Results and discussion

4.1. Isothermal D–E loops

Figure 4 plots the isothermal bipolar *D–E* loops measured at temperatures between (a) 40 and 250 °C for 5/65/35 PLZT

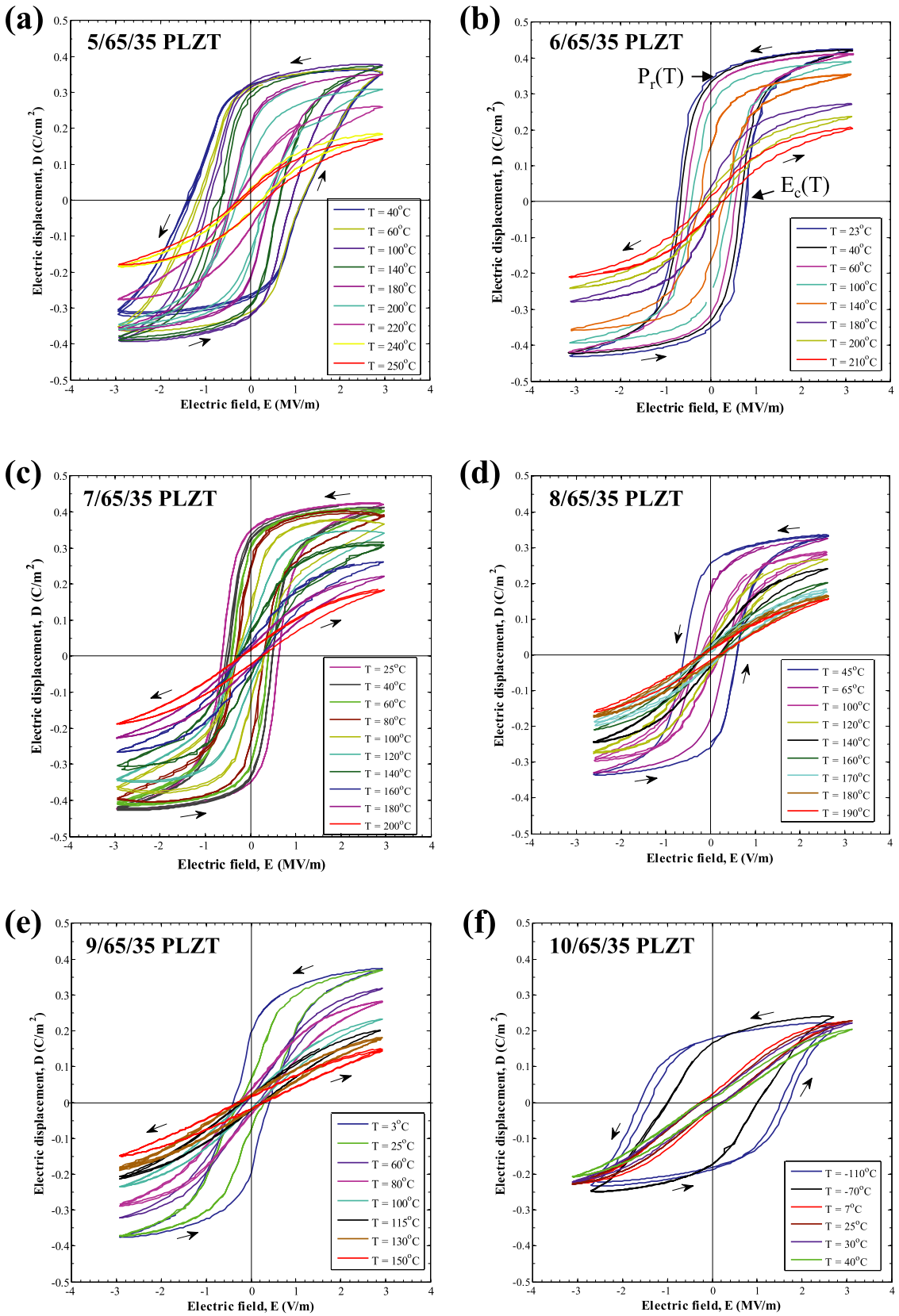

Figure 4. Bipolar isothermal electric displacement versus electric field (*D–E*) hysteresis curves measured at 0.1 Hz for (a) 5/65/35 PLZT, (b) 6/65/35 PLZT, (c) 7/65/35 PLZT, (d) 8/65/35 PLZT, (e) 9/65/35 PLZT, and (f) 10/65/35 PLZT at various temperatures. The temperatures corresponding to open loop ferroelectric behavior decreased as the lanthanum doping level *x* increased.

Sample 1, (b) 23 and 210 °C for 6/65/35 PLZT Sample 3, (c) 25 and 200 °C for 7/65/35 PLZT Sample 5, (d) 45 and 190 °C for 8/65/35 PLZT Sample 7 (e) 3 and 150 °C for 9/65/35 PLZT Sample 9, and (f) −110 and 40 °C for 10/65/35 PLZT Sample 11. The bipolar *D–E* loops were similar among samples of the same composition for any given temperature.

These measurements showed that the isothermal *D–E* loops overlapped and exhibited square ferroelectric behavior at relatively low temperatures when the remnant polarization was maximum. However, as the temperature increased, the isothermal *D–E* loops degenerated into narrow and linear loops [31]. Then, the remnant polarization gradually decreased and dropped sharply to ∼0.02 C m^{-2} beyond a critical temperature we will call the polarization transition temperature denoted by T_p. Similarly, figure 4 indicates that the coercive field E_C decreased with increasing temperature for all compositions. This behavior was attributed to rapid dipole fluctuations at high temperatures contributing to the energy required for polarization switching. Moreover, the coercive fields were smaller for 9/65/35 PLZT than for 5/65/35 PLZT. This can be explained by a structural transformation from rhombohedral ferroelectric to slim loop cubic as the lanthanum doping level x increased from 5 to 9 mol% [40].

Note that the isothermal *D–E* loop of 10/65/35 PLZT at 25, 30, and 40 °C (figure 4(f)) were slim and featured small remnant polarization, characteristic of the relaxor phase. Moreover, the isothermal *D–E* loops of 10/65/35 PLZT did not exhibit open loop ferroelectric behavior until the temperature was lowered to −70 °C. Similar behavior was observed with 11/65/35 PLZT samples. Unfortunately, temperatures below 0 °C are unpractical for waste heat energy harvesting applications and therefore *x*/65/35 PLZT samples with $x \geq 10$ mol% were not considered further.

4.2. Polarization transition temperatures

Figure 5(a) shows the remnant polarization of *x*/65/35 PLZT at 0.1 Hz as a function of temperature for lanthanum doping level x between 5 and 10 mol%. The solid lines represent polynomial fits and are plotted to guide the eye. The remnant polarization was large in the ferroelectric state for each composition. This was the manifestation of the cooperative ordering of dipole orientation at low temperature [37]. However, the remnant polarization decreased with increasing temperature until it reached negligibly small values ($P_r \leq$ 0.02 C m^{-2}) beyond the polarization transition temperature T_p. The small remnant polarization at high temperatures was evidence of the dipole disorder induced by thermal fluctuations. Note that the remnant polarization $P_r(T)$ of ferroelectric relaxors retained finite values above T_p due to the persistence of nanopolar domains interacting with each other at temperatures between T_p and T_B [52].

Figure 5(b) plots the *x*/65/35 PLZT polarization transition temperature T_p for lanthanum doping level x between 5 and 10 mol%. The values of T_p are also summarized in table 1. Figure 5(b) shows that the polarization transition

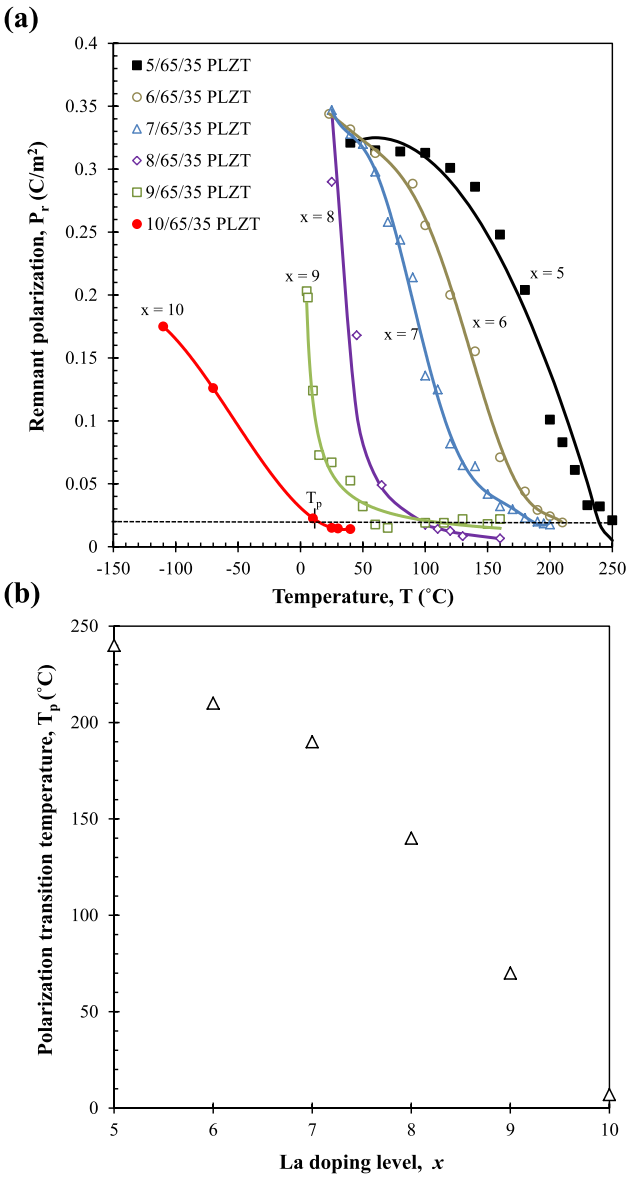

Figure 5. (a) Remnant polarization extracted from isothermal *D–E* loops measured at 0.1 Hz as a function of temperature for various *x*/65/35 PLZT compositions with x between 5 and 10 mol%. Solid lines represent polynomial fits and are plotted to guide the eye. The remnant polarization $P_r(T)$ corresponds to the polarization under zero applied electric field. (b) Polarization transition temperature T_p of *x*/65/35 PLZT as a function of lanthanum doping level x varying from 5 to 10 mol%. We define the polarization transition temperature T_p as the temperature corresponding to a negligibly small remnant polarization ($P_r \leq$ 0.02 C m^{-2}).

temperature decreased from 240 to 10 °C as the molar fraction of lanthanum dopant increased from 5 to 10 mol%. In order to achieve a large change in electric displacement necessary to obtain a large energy density, the Olsen cycle should be performed on PLZT samples between T_{cold} and $T_{hot} > T_p$. This suggests that these different PLZT compositions should be operated over different temperature ranges to achieve maximum thermal to electrical energy conversion.

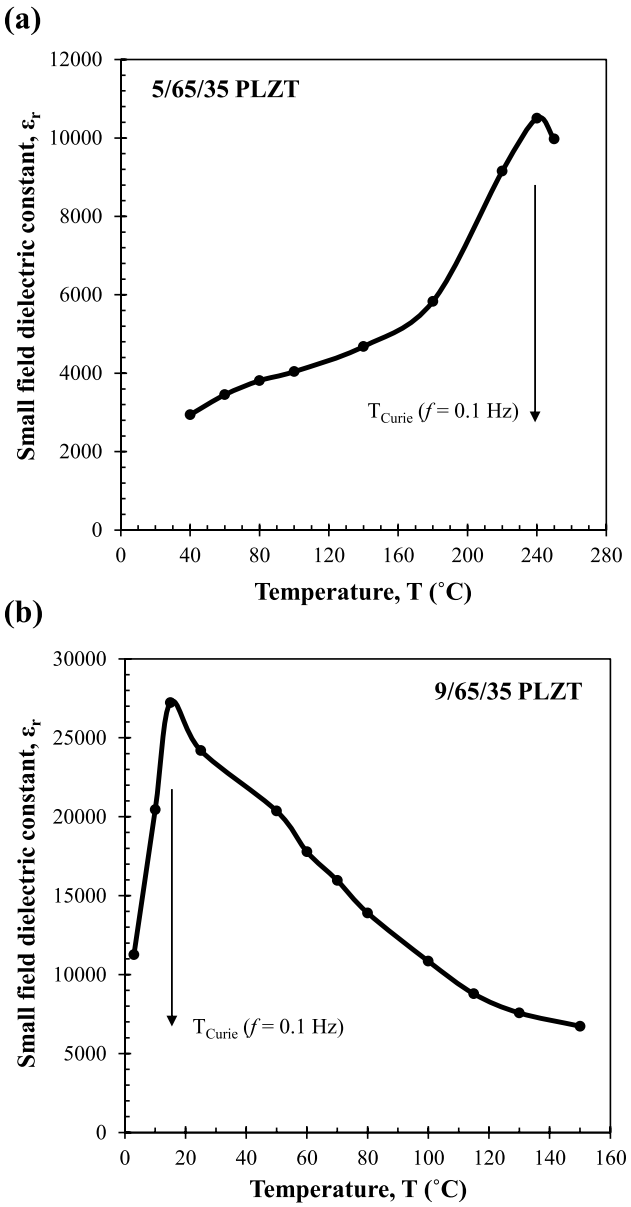

Figure 6. Small field dielectric constant $\varepsilon_r(E, T)$ for (a) 5/65/35 PLZT and (b) 9/65/35 PLZT as a function of temperature retrieved from isothermal bipolar D–E loops measured at 0.1 Hz as the slope of the linear fit corresponding to isothermal field reduction from $E_{cr}(T)$ to 0 MV m^{-1}. The Curie temperature at 0.1 Hz was identified as the temperature corresponding to the maximum value of ε_r.

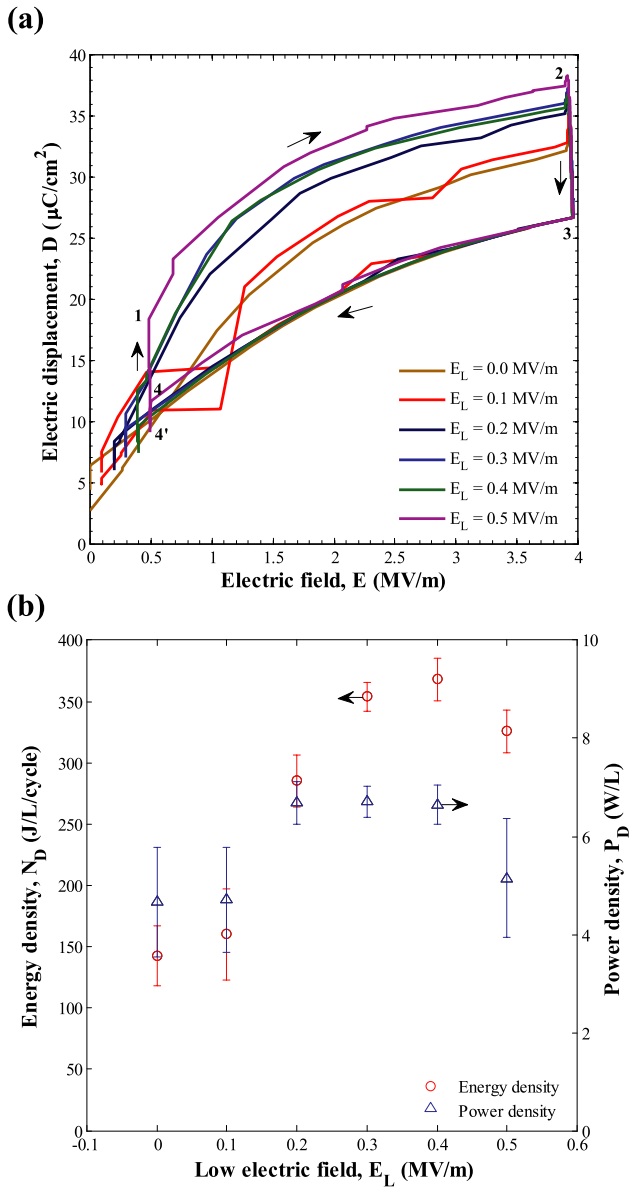

Figure 7. (a) Experimental Olsen cycle in the D–E diagram performed on 9/65/35 PLZT Sample 10 between T_{cold} = 3 °C and T_{hot} = 150 °C for E_H = 4.0 MV m^{-1} and E_L varying from 0 to 0.5 MV m^{-1}. The Olsen cycles were vertically displaced to coincide at T_{hot} and E_H (state 3). (b) The corresponding energy and power densities generated with Sample 10 for five different Olsen cycles performed under the above conditions. A peak in energy density was reached at $E_L^* = 0.4$ MV m^{-1} while a peak in power density was obtained for $E_L^+ = 0.2$ MV m^{-1}.

4.3. Curie temperature

The Curie temperature is typically defined as the temperature corresponding to the maximum dielectric constant. Figure 6 plots the small field dielectric constant of (a) 5/65/35 PLZT and (b) 9/65/35 PLZT at 0.1 Hz as a function of temperature. They were retrieved from the isothermal bipolar D–E loops as the slope of the linear fit corresponding to an isothermal field reduction from $E_{cr}(T)$ extrapolated to 0 MV m^{-1}. Table 1 presents the Curie temperature of x/65/35 PLZT for x between 5 and 9 mol%. Dielectric constant measurements for 5/65/35 PLZT at 0.1 Hz show that the Curie temperature T_{Curie} was similar to the polarization transition temperature T_p and equal to 240 °C. This is consistent with the fact that classical ferroelectric materials including 5/65/35 PLZT do not exhibit frequency dispersion [67]. However, for 9/65/35 PLZT, the Curie temperature T_{Curie} = 15 °C fell below the polarization transition temperature estimated as T_p = 70 °C at 0.1 Hz. This can be attributed to the pronounced frequency dispersion featured in relaxor–ferroelectric x/65/35 PLZT compositions for $x \geq 7$ mol% as discussed in [47]. In fact, the Curie temperature of relaxor–ferroelectric materials is frequency-dependent and shifts to higher values with increasing frequency [67].

Table 2. Maximum energy and power densities achieved using the Olsen cycle for different materials, temperature ranges, operating electric fields, and cycle frequencies.

Sample	Material	T_{cold} (°C)	T_{hot} (°C)	E_L^* (MV m^{-1})	E_H (MV m^{-1})	f (Hz)	$N_{D,max}$ (J l^{-1} per cycle)
1	5/65/35 PLZT	40	250	0.4	7.5	0.0296	799.5 ± 11.3
3	6/65/35 PLZT	40	210	0.4	8.5	0.0353	949.3 ± 11.2
5	7/65/35 PLZT	30	200	0.2	7.0	0.0256	1013.5 ± 16.2
7	8/65/35 PLZT	25	160	0.2	7.5	0.0178	887.5 ± 8.5
9	9/65/35 PLZT	3	150	0.4	7.5	0.0191	653.5 ± 34.3
Sample	Material	T_{cold} (°C)	T_{hot} (°C)	E_L^+ (MV m^{-1})	E_H (MV m^{-1})	f (Hz)	$P_{D,max}$ (W l^{-1})
2	5/65/35 PLZT	40	250	0.4	9.0	0.0656	41.8 ± 2.2
4	6/65/35 PLZT	40	210	0	8.5	0.0604	47.9 ± 1.0
6	7/65/35 PLZT	30	200	0	9.5	0.0839	47.5 ± 0.3
8	8/65/35 PLZT	25	160	0.2	9.0	0.0627	39.5 ± 2.0
10	9/65/35 PLZT	3	150	0.2	7.0	0.0710	35.9 ± 0.6

4.4. Effect of low electric field E_L

Table 2 summarizes the operating temperature ranges, applied electric fields, and maximum energy and power densities generated in the present study by subjecting PLZT ceramics with various lanthanum doping concentrations to the Olsen cycle. Figure 7(a) plots six different Olsen cycles on the *D–E* diagram executed on 9/65/35 PLZT Sample 10 with low electric field E_L equal to 0, 0.1, 0.2, 0.3, 0.4, and 0.5 MV m^{-1}. This composition was selected for illustration purposes. The high electric field E_H was set as 4.0 MV m^{-1} while the cold and hot source temperatures were maintained at 3 and 150 °C, respectively. Due to the measurement method of electric displacement D in the Olsen cycle, it was only possible to measure changes in electric displacement rather than absolute displacement. Therefore, the Olsen cycles shown were vertically translated to coincide at T_{hot} and E_H (state 3).

Figure 7(b) shows the energy density and power density generated by Sample 10 as a function of E_L ranging between 0 and 0.5 MV m^{-1} corresponding to data shown in figure 7(a). The error bars correspond to two standard deviations or a 95% confidence interval. Those associated with P_D accounted for uncertainties for both energy density N_D and frequency f and were estimated from error propagation analysis. This explains why the errors bars for P_D are larger than those for N_D. It is evident that the energy density reached a maximum at $E_L^* = 0.4$ MV m^{-1}. As E_L decreased from 0.4 to 0 MV m^{-1}, a sharp decrease in the average energy density from 368.2 to 143.0 J l^{-1} per cycle was observed. This reduction can be explained by the fact that the sample was unable to re-polarize at zero electric field when the temperature decreased from T_{hot} to T_{cold} (Process 4-1). Unfortunately, de-poling the sample below or near the coercive field $E_C = 0.09$ MV m^{-1} at $T_{hot} =$ 150 °C resulted in crossovers in the Olsen cycle *D–E* curve between processes 1-2 and 3-4 as shown in figure 7(a) ($E_L =$ 0 MV m^{-1}) and a smaller energy density. Meanwhile, raising the low electric field E_L from 0.4 to 0.5 MV m^{-1} reduced the average energy density from 368.2 to 325.7 J l^{-1} per cycle. This was due to the smaller electric field span ($E_H - E_L$) imposed in the Olsen cycle. Similarly, figure 7(b) shows that the largest power density was obtained for the low electric field set as $E_L^+ = 0.2$ MV m^{-1}. However, the power densities achieved with low electric fields $E_L = 0.2$, 0.3, and 0.4 MV m^{-1} were found to be relatively similar and within the experimental uncertainty of 0.036 W l^{-1} corresponding to a maximum difference of 1%. Similar results were obtained for other PLZT compositions. The values of E_L^* and E_L^+ for each composition are summarized in table 2.

4.5. Effect of high electric field E_H

Figure 8 plots the energy densities generated by *x*/65/35 PLZT as a function of high electric field E_H ranging from 3.0 to 9.5 MV m^{-1} for $5 \leq x \leq 9$ mol%. In all cases, E_L was set to E_L^*, previously estimated. Similarly, the optimum temperatures T_{cold} and $T_{hot} \geq T_{Curie}$ for each composition were imposed, as summarized in table 2. Figure 8 indicates that raising the electric field span ($E_H - E_L^*$) resulted in larger energy densities. For example, the average energy density generated by a 190 μm thick 7/65/35 PLZT sample increased by 51% from 553.0 to 832.8 J l^{-1} per cycle as the high electric field E_H increased from 4.0 to 6.0 MV m^{-1} (figure 8(c)). However, the maximum value of E_H was limited by the samples' dielectric breakdown. Cracks formed within the sample beyond an applied electric field threshold. The formation of cracks may be attributed to mechanical stresses in the material along the grain boundaries due to spatially variant electric fields causing preferential domain wall motion [68]. Microcracks may then propagate along the grain boundaries of the sample under the cyclic electric field loading/unloading. Ultimately, the field-induced crack propagation led to sample failure.

Figure 8(c) also shows that the energy density of 7/65/35 PLZT increased with increasing high electric field E_H up to 7.0 MV m^{-1} and then decreased for $E_H = 8.0$ MV m^{-1}. This can be attributed to a significant increase in leakage current at large electric fields. Samples of other compositions investigated in this study were unable to withstand electric field large enough to observe this behavior.

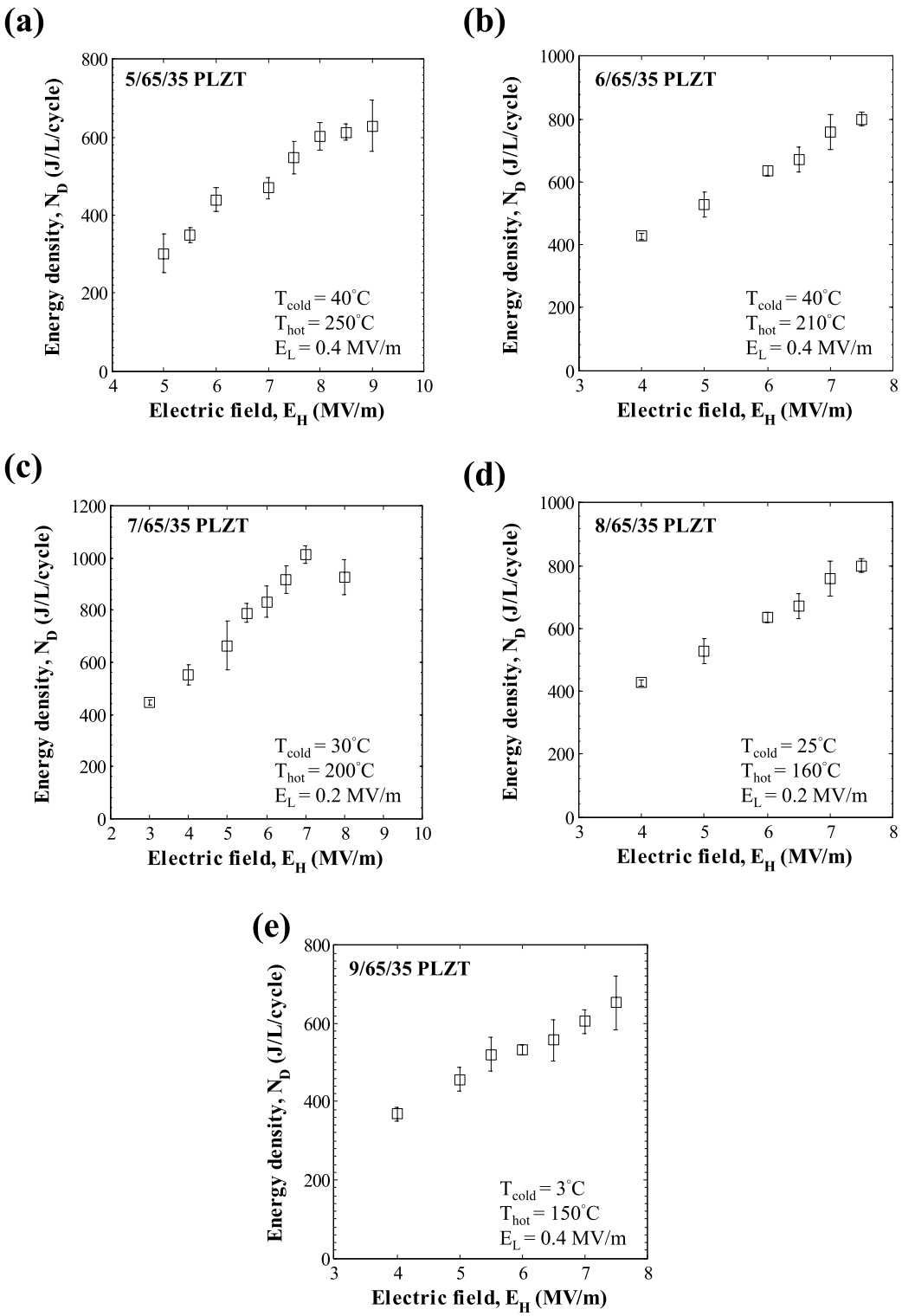

Figure 8. Experimentally measured energy density produced by (a) 5/65/35 PLZT, (b) 6/65/35 PLZT, (c) 7/65/35 PLZT, (d) 8/65/35 PLZT, and (e) 9/65/35 PLZT as a function of high electric field for Olsen cycles performed under quasiequilibrium conditions with $E_{\mathrm{L}} = E_{\mathrm{L}}^{*}$ and the optimum temperatures T_{cold} and T_{hot} for each composition.

4.6. Maximum energy density

Figure 8(c) also shows that a maximum energy density of 1013.5 $\pm$ 16.2 J l^{-1} per cycle, corresponding to a power density of 25.9 ± 0.8 W l^{-1}, was obtained with 7/65/35 PLZT. The Olsen cycles were performed under quasiequilibrium conditions at 0.0256 Hz with electric field cycled between $E_{\mathrm{L}} = E_{\mathrm{L}}^{*} = 0.2$ MV m^{-1} and $E_{\mathrm{H}} = 7.0$ MV m^{-1}. The cold and hot source temperatures were equal to $T_{\mathrm{cold}} = 30\,^{\circ}\mathrm{C}$ and $T_{\mathrm{hot}} = 200\,^{\circ}\mathrm{C}$, respectively. To the best of our knowledge, this

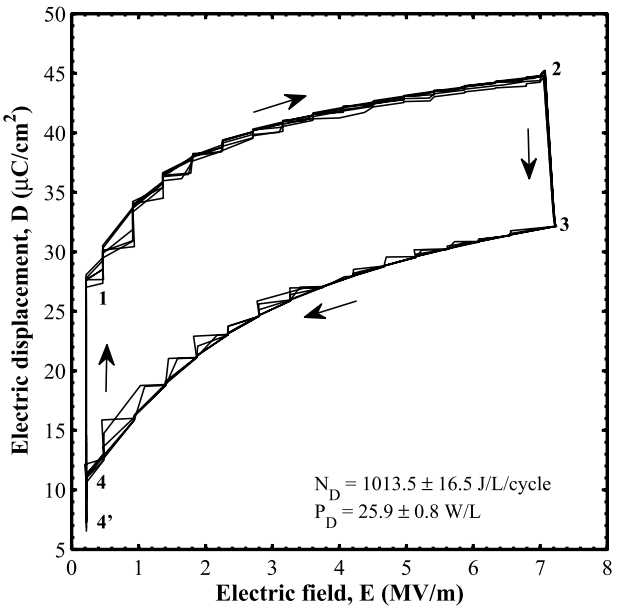

Figure 9. Electric displacement versus electric field diagram for six experimental Olsen cycles using 7/65/35 PLZT Sample 5. The electric field was cycled between $E_L = E_L^* = 0.2$ MV m^{-1} and $E_H = 7.0$ MV m^{-1} while the temperature varied between $T_{cold} = 30\,^{\circ}$C and $T_{hot} = 200\,^{\circ}$C. The average energy density over six cycles was 1013.5 ± 16.2 J l^{-1} per cycle at 0.0256 Hz, corresponding to the largest energy density achieved in this study.

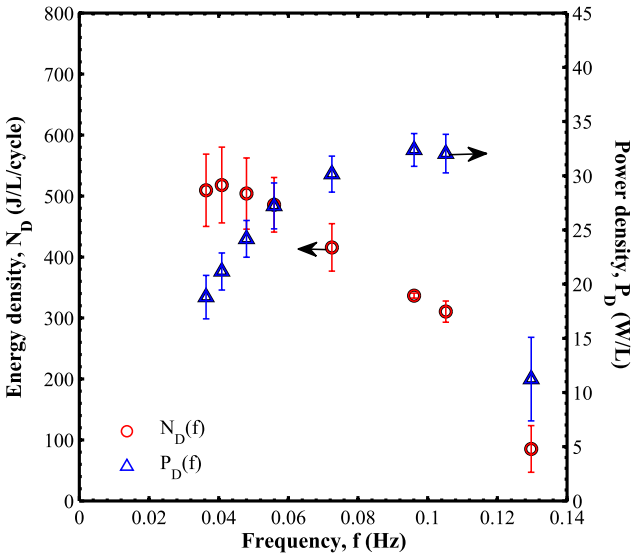

Figure 10. Energy and power densities obtained with 9/65/35 PLZT Sample 10 as a function of cycle frequency for $E_L = 0.2$ MV m^{-1} and $E_H = 6.0$ MV m^{-1} with $T_{cold} = 3\,^{\circ}$C, and $T_{hot} = 150\,^{\circ}$C. The durations τ_{12} and τ_{34} were equal and fixed at around 1.5 s. The durations τ_{23} and τ_{41} of isoelectric field processes 2-3 and 4-1 were equal and ranged from about 2 to 15 s. The energy density and the power density reached a maximum at 0.0364 and 0.0961 Hz, respectively.

energy density is the largest achieved using the Olsen cycle among pyroelectric single crystals, ceramics, and polymeric materials reported to date.

Figure 9 presents six consecutive Olsen cycles on the *D–E* diagram corresponding to this maximum energy density. The *D–E* paths of the Olsen cycles were not closed since Points 4 and 4′ did not coincide. The offset between points 4′ and 4 can be explained by the leakage current observed across the PLZT ceramic at high temperatures and/or large electric fields [7, 18, 69, 70] as previously discussed. Note that the Olsen cycles plotted in figure 9 did not follow a smooth path between E_L and E_H during isothermal processes 1-2 and 3-4 in the *D–E* diagram. This was likely due to microcracks propagating along the grain boundaries of the sample while the Olsen cycle was performed under high electric fields and/or high temperatures [71]. These fractures introduced spatial variations in the local electric field near the crack front resulting in sample inhomogeneity [72].

4.7. Effect of cycle frequency f

For illustration purposes, figure 10 plots both the energy and power densities obtained with 9/65/35 PLZT as a function of cycle frequency for $E_L^+ = 0.2$ MV m^{-1} and $E_H = 6.0$ MV m^{-1}. The cold and hot temperatures were $T_{cold} = 3\,^{\circ}$C and $T_{hot} = 150\,^{\circ}$C, respectively. The four different processes in the Olsen cycle performed at frequencies below 0.036 Hz corresponded to quasiequilibrium conditions. Figure 10 indicates that, under the above conditions, the energy density reached a maximum of 509.4 ± 29.6 J l^{-1} per cycle at 0.036 Hz and then decreased with increasing cycle frequency. The rise in N_D can be explained by the excessive leakage current observed in the material with frequency below 0.036 Hz. In fact, smaller frequencies provided sufficient time for charges at the surface of the PE to conduct through its body (leakage current) particularly under large applied electric field and/or high operating temperature. The leakage current can be estimated from the surface area of the triangle defined by 4, 3, and 4′. For 9/65/35 PLZT, the loss in energy density associated with the leakage current was estimated to be 10% and 20% when the Olsen cycle was performed at 0.036 Hz and 0.02 Hz, respectively. On the other hand, as the cycle frequency increased beyond 0.036 Hz, the energy density decreased due to a reduction in electric displacement span as the processes were not performed under quasiequilibrium conditions (i.e. the Olsen cycle did not span the isothermal *D–E* loops).

Figure 10 also indicates that under the above described operating conditions, the power density P_D from 9/65/35 PLZT reached a maximum of 32.4 ± 0.8 W l^{-1} at the peak power frequency of 0.096 Hz. Performing the Olsen cycle at frequencies greater than 0.096 Hz led to a smaller power output. This behavior may be explained by considering the relaxation and heat transfer mechanisms. First, the dipole realignment occurring during the isoelectric field heating and cooling processes 2-3 and 4-1 did not have time to complete at frequencies larger than 0.096 Hz due to the slow dipole relaxation inherent to ferroelectric–relaxor materials, particularly at temperatures below T_{Curie} [73]. This is caused by the high energy barrier required to reorient the frozen nanodomains at low temperatures [74]. Second, the samples were unable to reach thermal equilibrium when the Olsen

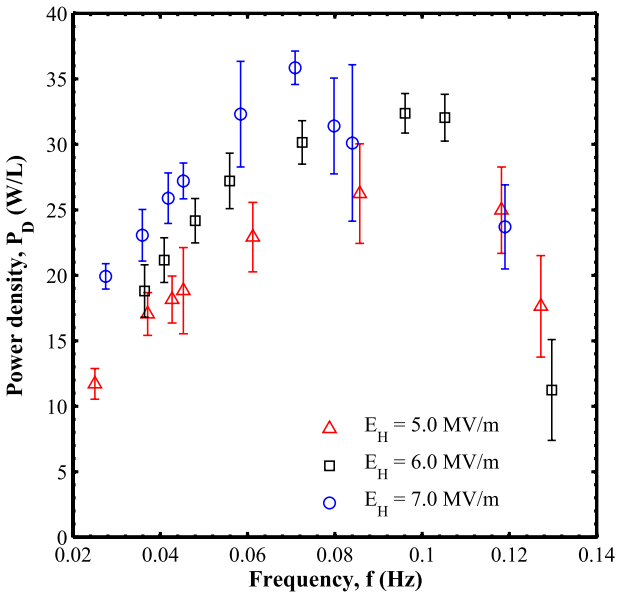

Figure 11. Power density generated by 9/65/35 PLZT Sample 10 as a function of cycle frequency between 0.02 and 0.13 Hz. The low electric field E_L was set as 0.2 MV m^{-1} while the high electric field E_H was set as either 5.0, 6.0, or 7.0 MV m^{-1}. The cold and hot source temperatures were equal to $T_{cold} = 3\,^{\circ}C$ and $T_{hot} = 150\,^{\circ}C$, respectively. The peak power frequency was equal to 0.0859, 0.0961, and 0.0709 Hz for high electric field E_H equal to 5.0, 6.0, and 7.0 MV m^{-1}, respectively.

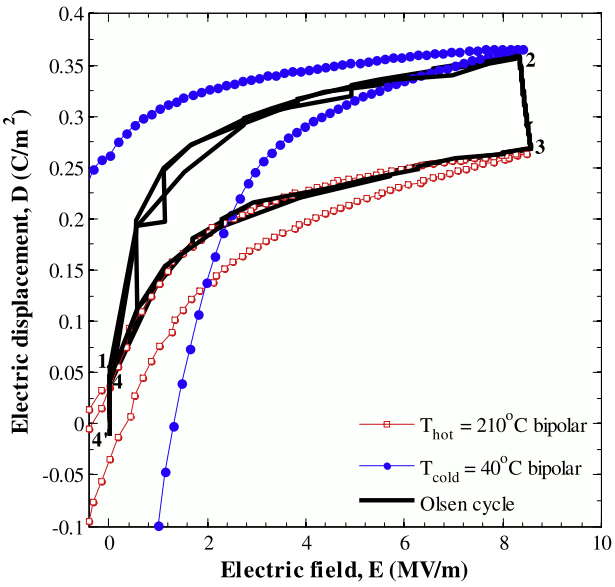

Figure 12. *D–E* diagram of isothermal bipolar *D–E* loops collected on 6/65/35 PLZT Sample 4 at $T_{cold} = 40\,^{\circ}C$ and $T_{hot} = 210\,^{\circ}C$ overlaid with three consecutive Olsen cycles performed at 0.0604 Hz with the electric field cycled between $E_L = 0.4$ MV m^{-1} and $E_H = 8.5$ MV m^{-1}. The average power density generated over three cycles was 47.8 ± 1.0 W l^{-1}, representing the largest power output in the present study. The Olsen cycles were vertically displaced to coincide with the isothermal *D–E* curve at T_{hot}.

cycle was performed at large cycle frequencies. In other words, the temperature swings of the pyroelectric material did not reach the temperature of the oil baths during processes 2-3 and 4-1. Therefore, phase transitions may be incomplete resulting in a smaller electric displacement span and electrical energy and power output. Although the energy density generated by Sample 10 decreased from 509 to 336 J l^{-1} per cycle as the frequency increased from 0.036 to 0.096 Hz, the corresponding power density increased from 18.8 to 32.4 W l^{-1}. This confirms that $P_D = N_D(f)f$ reaches a maximum through a compromise between large frequency f and energy density N_D.

Figure 11 plots the power density generated by 9/65/35 PLZT Sample 10 as a function of cycle frequency between 0.02 and 0.13 Hz. The low electric field was set as $E_L = E_L^+ = 0.2$ MV m^{-1} while the high electric field E_H was set at 5.0, 6.0, or 7.0 MV m^{-1}. The cold and hot source temperatures were $T_{cold} = 3\,^{\circ}C$ and $T_{hot} = 150\,^{\circ}C$, respectively. Figure 11 indicates that the peak power density increased with increasing high electric field E_H. This is attributed to (i) the increase in energy density N_D due to larger electric field span ($E_H - E_L^+$) and (ii) the increase in the time rate of change of the electric field for a given cycle frequency f. Figure 11 also indicates that the peak power density was reached at 0.0859, 0.0961, and 0.0709 Hz for high electric field E_H equal to 5.0, 6.0, and 7.0 MV m^{-1}, respectively. However, the variations in power density near these frequencies (±0.01 Hz) were small. The differences in peak power frequency were attributed to experimental uncertainties. In order to ensure that the material did not break prematurely due to large thermoelectromechanical stress, the high electric field was imposed to $E_H = 5.0$ MV m^{-1} to determine the peak power frequency for testing the other PLZT compositions as summarized in table 2.

4.8. Maximum power density

Figure 12 presents isothermal bipolar *D–E* loops collected on 6/65/35 PLZT sample 4 at $T_{cold} = 40\,^{\circ}C$ and $T_{hot} = 210\,^{\circ}C$ overlaid with three consecutive Olsen cycles performed at 0.0604 Hz with the electric field cycled between $E_L = E_L^+ = 0$ MV m^{-1} and $E_H = 8.5$ MV m^{-1}. These Olsen cycles correspond to the largest power density obtained in this study with any PLZT composition investigated. This was due to smaller leakage current observed in 6/65/35 PLZT and its ability to re-polarize at $T_{cold} = 40\,^{\circ}C$ under zero bias electric field since these conditions were not near a ferroelectric–relaxor phase boundary, unlike the other compositions. This enabled the isoelectric field cooling process to be performed rapidly resulting in larger frequency.

Figure 12 also shows that process 3-4 of the Olsen cycle follows the decreasing electric field path of the isothermal *D–E* loop at T_{hot}. However, process 1-2 did not follow the increasing electric field path of the isothermal *D–E* loop at T_{cold}. This may be attributed to the existence of mixed ferroelectric and ergodic relaxor phases [30, 75] when the applied electric field increased from E_L to $E_{cr}(T)$ at T_{cold}. These phases co-existed likely due to slow stabilization of the ferroelectric phase from the relaxor phase caused by parasitic interactions between defects and polar nanoregions [75].

4.9. Discussion

Table 2 indicates that the maximum energy density was reached for all compositions at frequencies between 0.019 and 0.035 Hz. On the other hand, the maximum power output was obtained at higher frequencies between 0.060 and 0.084 Hz. Additionally, the optimum value of E_H imposed for different samples was not the same. This is likely due to the different electric field breakdown inherent to the different compositions and to sample variation caused by parasitic defects introduced during the material synthesis process.

The maximum energy densities of *x*/65/35 PLZT with *x* ranging from 5 to 9 mol% outperformed those reported for single crystal PMN-32PT [35] and PZN-4.5PT [66] by a factor of four to seven and were nearly twice as large as those obtained with copolymer 60/40 P(VDF-TrFE) [18]. The larger remnant and saturation polarization of PLZT enabled larger electric displacement span in the Olsen cycle thus increasing energy density N_D as suggested by equation (2). Furthermore, using PLZT ceramics offers advantages over 60/40 P(VDF-TrFE) in that PLZT (i) possesses significantly lower leakage current thanks to their higher electrical resistivity, (ii) does not require electrical poling prior to performing the Olsen cycle [18, 34, 69], (iii) requires smaller electric field E_H in the Olsen cycle, namely $\sim$10 MV m^{-1} for PLZT versus $\sim$50 MV m^{-1} for 60/40 P(VDF-TrFE) [18], and (iv) is capable of withstanding higher temperatures without melting thus rendering it suitable for temperature up to 250 °C.

The achievable energy and power densities of PLZT could be further increased by increasing the electrical breakdown strength of the material. One way is by reducing its porosity. Yin *et al* [76] reported the porosity of PLZT ceramics synthesized by the mixed oxide method to be around 5%. Indeed, pores act as pins against domain formation and movement [76]. They tend to concentrate high mechanical stress and therefore reduce the materials' dielectric strength [33]. The porosity of PLZT ceramics can be reduced to less than around 1% by synthesizing samples using the isostatic hot-press method [76]. This method consists of simultaneously imposing a high temperature and external pressure during the sintering process. This procedure enhances particle packing and reduces the number and size of pores, thus increasing the samples' dielectric breakdown strength [76]. Another way to increase the dielectric breakdown strength of PLZT samples is by fabricating samples with thickness on the order of nano- to micro-meters as they are capable of withstanding large electric field without sample failure [40]. The use of thin film PLZT on substrates would also substantially reduce the applied voltage delivered to the electrical circuit during the Olsen cycle. For example, only 8 V applied across a 10 μm thin PLZT film would be required to achieve an electric field of 8.0 MV m^{-1} instead of 1600 V required across a 200 μm thick sample. Then, the Olsen cycle could be easily implemented in devices.

Moreover, using thin films reduces the thermal time constant and, in principle, shortens the duration required for samples to reach thermal equilibrium during isoelectric field processes 2-3 and 4-1. For example, reducing the specimen film thickness from 200 to 10 μm decreases the thermal time constant in the dipping experiments from 1.7 to less than 0.1 s.

5. Conclusion

This paper reported experimental measurements of the energy and power densities generated by the relaxor–ferroelectric *x*/65/35 PLZT system subjected to the Olsen cycle. PLZT thin films with various compositions were synthesized by the mixed oxide method and their temperature-dependent dielectric behavior was characterized. The polarization temperature and Curie temperature of the different *x*/65/35 PLZT compositions were found to increase with lanthanum doping level *x*. Large energy and power densities were obtained by performing the Olsen cycle on PLZT samples undergoing an ergodic relaxor–ferroelectric phase transition. A maximum energy density of 1014 $\pm$ 16 J l^{-1} per cycle was produced by 7/65/35 PLZT under quasiequilibrium conditions. To the best of our knowledge, this is the largest energy density generated by any pyroelectric materials to date. A maximum power density of 48$\pm$1 W l^{-1} was obtained from 6/65/35 PLZT at 0.060 Hz. The *x*/65/35 PLZT compositions with *x* ranging from 5 to 9 mol% can be used in multistage devices operating between 70 and 240 °C.

Acknowledgment

F Lee expresses appreciation to the UCLA Mechanical and Aerospace Engineering Department for financial support in the form of a Graduate Fellowship.

References

[1] Chen H, Goswami D Y and Stefanakos E K 2010 A review of thermodynamic cycles and working fluids for the conversion of low-grade heat *Renew. Sust. Energy Rev.* **14** 3059–67

[2] Lawrence Livermore National Laboratory 2011 *US Energy Flow Trends—2009* September 16 https://publicaffairs.llnl.gov/news/energy/energy.html#2009

[3] Kouchachvili L and Ikura M 2006 Pyroelectric conversion—effects of P(VDF-TrFE) preconditioning on power conversion *J. Electrostat.* **65** 182–8

[4] Hunter S, Lavrik N, Bannuru T, Mostafa S, Rajic S and Datskos P 2011 Development of MEMS based pyroelectric thermal energy harvesters *Proc. SPIE* **8035** 80350V

[5] Thombare D G and Verma S K 2008 Technological development in the Stirling cycle engines *Renew. Sust. Energy Rev.* **12** 1–38

[6] Liu B T, Chien K H and Wang C C 2004 Effect of working fluids on organic Rankine cycle for waste heat recovery *Energy* **29** 1207–17

[7] Kouchachvili L and Ikura M 2008 Improving the efficiency of pyroelectric conversion *Int. J. Energy Res.* **32** 328–35

[8] Riffat S B and Ma X 2003 Thermoelectrics: a review of present and potential applications *Appl. Therm. Eng.* **23** 913–35

[9] Olsen R B, Bruno D A, Briscoe J M and Butler W F 1981 A pyroelectric energy converter which employs regeneration *Ferroelectrics* **38** 1–4

[10] Olsen R B 1982 Ferroelectric conversion of heat to electrical energy—a demonstration *J. Energy* **6** 91–5

[11] Olsen R B and Brown D D 1982 High-efficiency direct conversion of heat to electrical energy-related pyroelectric measurements *Ferroelectrics* **40** 17–27

[12] Olsen R B and Bruno D A 1986 Pyroelectric conversion materials *Proc. 21st Intersociety Energy Conversion Engineering Conf.* (San Diego, CA: American Chemical Society) pp 89–93

[13] Olsen R B, Bruno D A and Briscoe J M 1984 Cascaded pyroelectric energy converter *Ferroelectrics* **59** 205–19

[14] Olsen R B, Bruno D A and Briscoe J M 1985 Pyroelectric conversion cycles *J. Appl. Phys.* **58** 4709–16

[15] Ikura M 2002 Conversion of low-grade heat to electricity using pyroelectric copolymer *Ferroelectrics* **267** 403–8

[16] Kouchachvili L and Ikura M 2004 *US Patent Specification #7,323,506* issued 1/29/2008, filed

[17] Navid A, Vanderpool D, Bah A and Pilon L 2010 Towards optimization of a pyroelectric energy converter for harvesting waste heat *Int. J. Heat Mass Transfer* **53** 4060–70

[18] Navid A and Pilon L 2011 Pyroelectric energy harvesting using Olsen cycles in purified and porous poly(vinylidene fluoride-trifuoroethylene) thin films *Smart Mater. Struct.* **20** 025012

[19] Sebald G, Seveyrat L, Guyomar D, Lebrun L, Guiffard B and Pruvost S 2006 Electrocaloric and pyroelectric properties of $0.75Pb(Mg_{1/3}Nb_{2/3})O_3$–$0.25PbTiO_3$ single crystals *J. Appl. Phys.* **100** 1–6

[20] Guyomar D, Pruvost S and Sebald G 2008 Energy harvesting based on FE-FE transition in ferroelectric single crystals *IEEE Trans. Ultrason. Ferroelectr. Freq. Control* **55** 279–85

[21] Khodayari A, Pruvost S, Sebald G, Guyomar D and Mohammadi S 2009 Nonlinear pyroelectric energy harvesting from relaxor single crystals *IEEE Trans. Ultrason. Ferroelectr. Freq. Control* **56** 693–9

[22] Zhu H, Pruvost S, Guyomar D and Khodayari A 2009 Thermal energy harvesting from $Pb(Zn_{1/3}Nb_{2/3})_{0.955}Ti_{0.045}O_3$ single crystals phase transitions *J. Appl. Phys.* **106** 124102

[23] Fang J, Frederich H and Pilon L 2010 Harvesting nanoscale thermal radiation using pyroelectric materials *ASME J. Heat Transfer* **132** 092701

[24] Nguyen H, Navid A and Pilon L 2010 Pyroelectric energy converter using co-polymer P(VDF-TrFE) and Olsen cycle for waste heat energy harvesting *Appl. Therm. Eng.* **30** 2127–37

[25] Cuadras A, Gasulla M and Ferrari V 2010 Thermal energy harvesting through pyroelectricity *Sensors Actuators* A **158** 132–9

[26] Mane P, Xie J, Leang K and Mossi K 2011 Cyclic energy harvesting from pyroelectric materials *IEEE Trans. Ultrason. Ferroelectr. Freq. Control* **58** 10–7

[27] Ravindran S K T, Huesgen T, Kroener M and Woias P 2011 A self-sustaining micro thermomechanic pyroelectric generator *Appl. Phys. Lett.* **99** 104102

[28] Lallart M, Cottinet P J, Guyomar D and Lebrun L 2012 Electrostrictive polymers for mechanical energy harvesting *J. Polym. Sci.* B **50** 523–35

[29] Lang S B and Das-Gupta D K 2001 *Handbook of Advanced Electronic and Photonic Materials and Devices* vol 4 (San Diego, CA: Academic)

[30] Safari A, Panda R K and Janas V F 2011 *Ferroelectric Ceramics: Processing, Properties and Applications* December 8 www.rci.rutgers.edu/∼ecerg/projects/ferroelectric.html

[31] Hooker M W 1998 *Properties of PZT-based piezoelectric ceramics between −150 and 250 °C* NASA/CR-1998–208708

[32] Moreno R C, James B A, Navid A and Pilon L 2012 Pyroelectric energy converter for harvesting waste heat: Simulations versus experiments *Int. J. Heat Mass Transfer* **55** 4301–11

[33] Navid A, Lynch C S and Pilon L 2010 Purified and porous poly(vinylidene fluoride-trifluoroethylene) thin films for pyroelectric infrared sensing and energy harvesting *Smart Mater. Struct.* **19** 055006

[34] Lee F Y, Navid A and Pilon L 2011 Pyroelectric waste heat energy harvesting using heat conduction *Appl. Therm. Eng.* **37** 30–7

[35] Kandilian R, Navid A and Pilon L 2011 The pyroelectric energy harvesting capabilities of PMN-PT near the morphotropic phase boundary *Smart Mater. Struct.* **20** 055020

[36] Lines M E and Glass A M 1977 *Principles and Applications of Ferroelectrics and Related Materials* (Oxford: Clarendon)

[37] Samara G A 2001 Ferroelectricity revisited-advances in materials and physics *Solid State Physics* vol 56 (San Diego, CA: Academic) pp 239–458

[38] Grindlay J 1970 *An Introduction to the Phenomenological Theory of Ferroelectricity* (London: Pergamon)

[39] Buchanan R and Huang J 1999 Pyroelectric and sensor properties of ferroelectric thin films for energy conversion *J. Eur. Ceram. Soc.* **98** 1467–71

[40] Dausch D E and Haertling G H 1996 The domain switching and structural characteristics of PLZT bulk ceramics and thin films chemically prepared from the same acetate precursor solutions *J. Mater. Sci.* **31** 3409–17

[41] Haertling G H and Land C E 1971 Hot-pressed $(Pb,La)(Zr,Ti)O_3$ ferroelectric ceramics for electro-optic applications *J. Am. Ceram. Soc.* **54** 1–11

[42] Bobnar V, Kutnjak Z, Pirc R and Levstik A 1999 Electric-field-temperature phase diagram of the relaxor ferroelectric lanthanum-modified lead zirconate titanate *Phys. Rev.* B **60** 6420–7

[43] Vodopivec B, Filipič C, Levstik A, Holc J and Kutnjak Z 2004 E–T phase diagram of the 6.5/65/35 PLZT incipient ferroelectric *J. Eur. Ceram. Soc.* **24** 1561–4

[44] Viehland D, Dai X H, Li J F and Xu Z 1998 Effects of quenched disorder on La-modified lead zirconate titanate: long and short-range ordered structurally incommensurate phases, and glassy polar clusters *J. Appl. Phys.* **84** 458–71

[45] Kamba S, Bovton V, Petzelt J, Rychetsky I, Mizaras R, Brilingas A, Banys J, Gringas J and Kosec M 2000 Dielectric dispersion of the relaxor PLZT ceramics in the frequency range 20 Hz–100 THz *J. Phys.: Condens. Matter* **12** 497–519

[46] Bokov A A and Ye Z G 2006 Recent progress in relaxor ferroelectrics with perovskite structure *J. Mater. Sci.* **41** 31–52

[47] Vodopivec B, Filipič C, Levstik A, Holc J and Kutnjak Z 2004 Dielectric properties of partially disordered lanthanum-modified lead zirconate titanate relaxor ferroelectrics *Phys. Rev.* B **69** 224208

[48] Dellis J L, El Marssi M, Tilloloy P, Farhi R and Viehland D 1997 A dielectric study of the *x*/65/35 lanthanum-modified lead zirconate titanate series *Ferroelectrics* **201** 167–74

[49] Xi Y, Zhili C and Cross L E 1983 Polarization and depolarization behavior of hot pressed lead lanthanum zirconate titanate ceramics *J. Appl. Phys.* **54** 3399–403

[50] Divya A S and Kumar V 2009 A novel mechanism for relaxor-ferroelectric transition in PLZT (8/65/35) *J. Am. Ceram. Soc.* **92** 2029–32

[51] Kutnjak Z, Filipič C, Pirc R and Levstik A 1999 Slow dynamics and ergodicity breaking in a lanthanum-modified lead zirconate titanate relaxor system *Phys. Rev.* B **59** 294–301

[52] Kholkin A 2010 Piezoresponse force microscopy of polarization dynamics in ferroelectrics *8th Int. Tutorial Workshop on Piezoresponse Force Microscopy and Nanoscale Electromechanics of Polar Materials (Beijing, Aug.)*

[53] Lee F Y, Goljahi S, McKinley I, Lynch C S and Pilon L 2012 Pyroelectric waste heat energy harvesting using relaxor ferroelectric 8/65/35/ PLZT and the Olsen cycle *Smart Mater. Struct.* **21** 025021

[54] Chin T, Lee F Y, McKinley I M, Goljani S, Lynch C S and Pilon L 2012 Direct thermal to electrical energy conversion using 9.5/65/35 PLZT ceramics in the ergodic relaxor phase *IEEE Trans. Ultrason. Ferroelectr. Freq. Control* **59** 2373–85

[55] Haertling G H and Buchanan R C (ed) 1991 *Ceramic Materials for Electronics: Processing, Properties, and Applications* (New York, NY: Dekker)

[56] Cha G and Ju S Y 2012 Electric field dependence of the curie temperature of ferroelectric poly(vinylidenefluoride-trifluoroethylene) co-polymers for pyroelectric energy harvesting *Smart Mater. Struct.* **21** 022001

[57] Zhu H, Pruvost S, Cottinet P J, Guyomar D and Lallart Mickael (ed) 2012 *Thermal Energy Harvesting Using Fluorinated Terpolymers, Small-Scale Energy Harvesting* (Rijeka: InTech)

[58] Gachigi K 1997 Electrical energy storage in antiferroelectric–ferroelectric switching, chemically modified lead zirconate ceramics *PhD Thesis* Pennsylvania State University

[59] Shah S and Ramachandra Rao M S 2000 Preparation and dielectric study of high-quality PLZT *x*/65/35 ($x = 6, 7, 8$) ferroelectric ceramics *Appl. Phys.* A **71** 65–9

[60] Chemicals M G 2012 *Technical Specifications Silicon Conformal Coating (Liquid) 422–1L/4L/20L Liquid* January 3 www.mgchemicals.com/downloads/pdf/specsheets/422l.pdf

[61] Clearco Products 2012 *Silicone Transformer Oil* May 14 www.clearcoproducts.com/silicone_transformer_oil.html

[62] Incropera F P, DeWitt D P, Bergman T and Lavine A 2006 *Fundamentals of Heat and Mass Transfer* 6th edn (New York, NY: Wiley)

[63] Santos I A, Endo C, Zanin A L, Lente M H, Eiras J A and Garcia D 2001 Hot-pressed transparent PLZT ceramics from low cost chemical processing *Mater. Res.* **4** 291–5

[64] Simhony M, Bass M, Van Stryland E, Tenescu E and Levy B 1979 Fast response of PLZT pyroelectric detectors to megawatt CO_2 laser pulses *IEEE J. Quantum Electron.* **15** 206–8

[65] Liščić B 2009 Heat transfer control during quenching *Mater. Manuf. Process.* **24** 879–86

[66] McKinley I, Kandilian R and Pilon L 2012 Waste heat energy harvesting using Olsen cycle on $0.945Pb(Zn_{1/3}Nb_{2/3})O_3$–$0.055PbTiO_3$ single crystals *Smart Mater. Struct.* **21** 035015

[67] Akbas M, Reaney I and Lee W 1996 Domain structure–property relations in lead lanthanum zirconate titanate ceramics *J. Mater. Res.* **11** 2293–301

[68] Wang D, Fotinich Y and Carman G P 1998 Influence of temperature on the electromechanical and fatigue behavior of piezoelectric ceramics *J. Appl. Phys.* **83** 5342–50

[69] Olsen R B, Bruno D A and Briscoe J M 1985 Pyroelectric conversion cycle of vinylidene fluoride-trifluoroethylene copolymer *J. Appl. Phys.* **57** 5036–42

[70] Yu J and Ikura M 2004 Direct conversion of low-grade heat to electricity using pyrorelectric conversion *Proc. 4th IASTED Int. Conf. European Power and Energy Systems (Rhodes)* pp 442–6

[71] Lynch C S 1998 Fracture of ferroelectric and relaxor electro-ceramics: influence of electric field *Acta Mater.* **46** 599–608

[72] Cao H and Evans A G 1994 Electric-field-induced fatigue crack growth in piezoelectrics *J. Am. Ceram. Soc.* **77** 1783–6

[73] Pavel M, Rychetsky I and Petzelt J 2001 Polar clusters in relaxor (Pb, La)(Zr, Ti)O_3 revealed by second harmonic generation *J. Appl. Phys.* **89** 5036–9

[74] Ye Z G 1996 Relaxor ferroelectric $Pb(Mg_{1/3}Nb_{2/3})O_3$: properties and present understanding *Ferroelectrics* **184** 193–208

[75] Filipič C, Vodopivec B, Holc J, Levstik A, Kutnjak Z and Beige H 2004 Relaxor and incipient ferroelectric phases in 6.5/65/35 PLZT ceramics *J. Eur. Ceram. Soc.* **24** 1565–8

[76] Yin Q, Zhu B and Zeng H 2009 *Microstructure, Property and Processing of Functional Ceramics* (New York, NY: Springer)